Honeycomb monolithic design to enhance the performance of Ni-based catalysts for dry reforming of methane

Fazia Agueniou, Hilario Vidal *, M. Pilar Yeste, Juan C. Hernández-Garrido, Miguel A. Cauqui, José M. Rodríguez-Izquierdo, José J. Calvino, José M. Gatica

Departamento de Ciencia de Materiales e Ingeniería Metalúrgica y Química Inorgánica, e IMEYMAT, Instituto Universitario de Investigación en Microscopía Electrónica y Materiales, Universidad de Cádiz, 11510 Puerto Real, Spain.

*Corresponding author

Tel. +34-956-012744

E-mail address: hilario.vidal@uca.es (Hilario Vidal)

23 **ABSTRACT**

24 Supported Ni catalysts (4.5 wt%) using a Ce-Zr oxide (18/82 molar ratio and a ceria-rich

25 surface) depicting advanced redox properties, were deposited by washcoating over

26 cordierite honeycombs (230 and 400 cpsi). FIB-STEM unveiled nanostructure details

27 otherwise undistinguishable by conventional techniques. The catalytic performance was

28 evaluated in the dry reforming of methane at 700-900 ºC, using a CH_4:CO_2 1:1 feedstock,

29 and exploring high Weight Hourly Space Velocity (115-346 L g^{-1} h^{-1}). The structured

30 catalysts exhibited better performance than the corresponding powders, reaching values

31 close to thermodynamic limits for both reactants conversion and H_2/CO ratio, from 750

32 ºC, and no deactivation was observed in prolonged experiments (24-48 hours). This was

33 related to both the high catalyst efficiency after being deposited with low loading on the

34 cordierite and the intrinsic advantages of the monolithic reactor, like preventing from the

35 kinetic control that operates in powdered samples under high WHSV or limiting the

36 deactivation.

37

38 **Keywords:** Nickel; Ceria-Zirconia; Dry Reforming of Methane; Honeycomb Cordierite;

39 FIB-(S)TEM.

40

41

1.   Introduction

Dry Reforming of Methane (DRM) is most likely one of the reactions that has attracted more attention in the last decade in the field of heterogeneous catalysis. This is due to the growing interest in syngas production processes [1], and the simultaneous abatement of two significant greenhouse gases such as CO_2 and CH_4 [2].

Although noble metals have been also employed [3], undoubtedly nickel-based catalysts have become the best option for this reaction because of their lower cost while keeping a high performance [4,5]. Nevertheless, it is well-known the tendency of nickel to suffer deactivation due to carbonaceous deposits originated in the reaction onto the metal surface. Among others, the appropriate selection of the support has been one of the most promising strategies to increase the stability of these catalysts [6]. Thus, for example, nickel has been supported over Ce-Zr and Ce-Pr mixed oxides, whose improved redox properties allow the oxidation of the carbon accumulated onto the metal [7,8]. A recent study explored the use as DRM catalysts of nickel supported onto Ce-Zr oxides previously activated to enhance their redox properties by using a thermo-chemical protocol consisting on a severe reduction at 950 ºC followed by a mild oxidation at 500 ºC [9]. Some of these formulations showed high activity and stability against deactivation caused by carbon formation even under very severe operating conditions.

However, in most published works dealing with DRM, catalysts are used in the form of powder, granules or pellets [10-14], as well illustrated even in the most recent reviews [5]. In contrast, the use in this process of structured catalysts is, so far, very scarcely reported; the only few works available having used either cordierite [15-18], silicon carbide [18] or stainless steel [19] honeycombs and, more rarely, membrane reactors [20]. This is doubly surprising if the well-known advantages of such design are considered [21], and also considering the precedents in the use of honeycomb monoliths

67 and foams in hydrocarbons reforming [22] and CO_2 methanation [23,24]. Moreover, in

68 the case of DRM, the conventional operation in diffusion mode would be favoured when

69 the catalyst consists in a thin coating of the ceramic walls. In addition, the open structure

70 of the honeycomb could minimize the overpressure or even blocking phenomena

71 produced by massive deposition of carbonaceous species, which eventually occur when

72 using powdered-packed reactors.

73   It is also important to consider that in the above cited works in which honeycomb

74 monoliths were employed for the DRM reaction, the studied structured catalyst was

75 obtained by wet impregnation of the monolith with precursor salts [15,18] or sol-gel

76 methods [18] and not by washcoating, which precludes any comparison between the

77 catalyst as a powder and after deposition on the monolith. The same approach was

78 followed in [16] where, additionally, a noble metal (Ru, 0.5% wt.) was used as promoter

79 of nickel. Regarding the study performed by Kohn et al. [17], the authors used a

80 commercial BASF catalyst (Rh/γ-Al_2O_3) as active phase loaded onto the monolith, but

81 did not provide any detail about its preparation. Finally, in [19] Fukuhara et al. did not

82 either consider the powder catalyst as a reference because the active phase, Ni doped with

83 Pd and Sn, used to coat a stainless-steel honeycomb substrate was obtained by an

84 electroless plating method.

85   Considering the background briefly revised above, the first purpose of this work

86 is to give a step forward by depositing a nickel-based advanced formulation onto

87 cordierite honeycombs using low specific loadings in order to maximize the advantages

88 of the structured design [15], testing them in the DRM reaction and making a comparison

89 with the same catalyst in the form of powder. Moreover, the monolithic design has

90 allowed us exploring experimental conditions, in terms of weight hourly space velocities

91 (WHSV), which have been rarely considered in previous works [5,25]. To rationalize the

92   results, an in-depth structural study by both macroscopic and atomic scale techniques was

93   carried out. Concerning the latter, a combination of Focused Ion Beam (FIB) electron

94   microscopy sample preparations with further analysis by Scanning Transmission Electron

95   Microscopy (STEM) has been used, previously proved as a quite powerful tool for the

96   characterization at the finest, subnanometric, and atomic, scales of coated honeycomb

97   monoliths and to understand their macroscopic performance [26,27]. Moreover, such

98   studies revealed that using this experimental approach it is possible to detect

99   microstructural features of the final catalytic device out of reach for other conventional

100   characterization techniques. Therefore, a second goal of this work is applying this

101   approach to investigate the prepared Ni-based honeycomb-type catalysts.

102   The work here presented deepens our preliminary communication [28] by

103   widening the set of samples investigated and applying the needed physico-chemical

104   techniques for a better understanding of the relationships between catalysts properties and

105   performance. Now we have included new reference samples to pay special attention to

106   the role played by the alumina employed for the structured catalysts preparation and the

107   effect of the honeycomb substrate cell density. Regarding the techniques, we have

108   incorporated results obtained by means of X-ray fluorescence, N_2 physisorption, X-Ray

109   Diffraction, H_2 and O_2 volumetric adsorption, TPR, and Temperature-Programmed

110   Reaction experiments followed by mass spectrometry. In this way, we can provide

111   information at compositional, textural, structural and chemical level, which is necessary

112   to explain the origin of the outstanding behaviour reported in our previous study [28].

113

114

115

116   **2.   Experimental**

5

117 *2.1.Powdered catalyst*

118   The ceria-zirconia support was prepared from a commercial nano-sized zirconia

119 from Tecnan-Nanomat S.L (78 $m^2 g^{-1}$ and 10-15 nm of BET and average particle size,

120 respectively) which was impregnated to incipient wetness with a $Ce(NO_3)_3 \cdot 6H_2O$

121 (99.99%, Sigma Aldrich) aqueous solution (0.88 M) to obtain an oxide having a 20%Ce-

122 80%Zr nominal molar composition. After drying in air (110 ºC, 12 h) and grinding (75

123 μm), the sample was calcined (500 ºC, 1 h). The resulting oxide was further activated for

124 its redox properties enhancement following a thermo-chemical aging protocol known as

125 SRMO (Severe Reduction-Mild Oxidation) proposed by our lab [29]. Briefly, it consists

126 in a reduction treatment under $H_2(5\%)/Ar$ (950 ºC, 2 h), followed by He flushing (950 ºC,

127 1 h) and oxidation with pulses of $O_2(5\%)/He$ at room temperature, and finally heating

128 under the oxidising mixture up to 500 ºC (1 h). In the following, the SRMO treated Ceria-

129 Zirconia oxide will be referred as CZ.

130   The supported nickel catalyst, named NiCZ, was prepared by incipient wetness

131 impregnation with a $Ni(NO_3)_2 \cdot 6H_2O$ (99.99%, Sigma Aldrich) aqueous solution (1.01 M)

132 aiming to reach a nominal 5 wt% metal loading. The catalytic precursor was dried (110

133 ºC, 12 h), calcined (400 ºC, 1 h) and finally grinded (75 μm).

134 *2.2.Honeycomb monolithic catalysts*

135   Cordierite blocks (Corning) with a cell density of 36 cells cm^{-2} (230 cpsi) or 62

136 cells cm^{-2} (400 cpsi), and wall thickness of 0.18 mm (7 mil) or 0.17 mm (6.5 mil),

137 respectively, were cut to obtain cylindrical pieces having 13 mm of diameter, 47 mm of

138 length and 2 g (230 cpsi samples) or 2.5 g (400 cpsi samples) of approximate weight.

139 Monolithic catalysts were prepared by washcoating from a slurry (stabilized at pH 4.0

140 using acetic acid) containing the NiCZ catalyst or the CZ support, following the

141 methodology well described by Prof. Montes laboratory [30]. The granulometry (d_{90} =

142   0.80 μm) and the Z potential (36 mV at pH = 4, with the isoelectric point at pH = 6.8)

143   data for the NiCZ sample are proper for the washcoating method as revised for example

144   in [30]. Therefore, we prepared slurries containing the NiCZ or the CZ sample (19.1

145   wt%), polyvinyl alcohol (1.7 wt%), Nyacol AL20 colloidal alumina (4.2 wt%) and water.

146   As far as our objective was to reach low catalyst loadings, we decided to prepare slurries

147   with low viscosity (5.1 mPa s). Cordierite pieces were immersed (3 cm min^{-1}) in this

148   slurry, kept fully immersed for 90 s, the first 15 s under ultra-sonication. They were

149   further pulled out at the same rate, and the excess of slurry was removed by air flowing.

150   The pieces were then dried at 120 ºC for 30 min and submitted to one or two new

151   coating/drying cycles until reaching the desired final specific loading, around 0.4 mg cm^{-2}

152   corresponding to a washcoat loading about 25 mg per g^{-1} of support. Finally, all the

153   monoliths were calcined (5 ºC min^{-1}) at 450 ºC (1 h).

154   The reached active phase loading was estimated from the weight gain after

155   calcination, and its adherence (expressed in percentage) from the weight loss after

156   immersion in petroleum ether under ultrasounds (30 min). The prepared monolithic

157   catalysts were named as H230 or H400 (according to the cell density of the cordierite)

158   followed by CZ or NiCZ (to denote the nature of the coating). The residual slurries,

159   containing either CZ or NiCZ, were dried and submitted to calcination at 450 ºC (1 h) to

160   obtain the CZ-S and NiCZ-S reference powdered samples, respectively.

161   *2.3. Catalysts characterization*

162   The prepared catalysts were characterized by ICP-AES using a Thermo Elemental

163   Iris Intrepid equipment. Complementary compositional analyses were performed through

164   X-ray micro-fluorescence (XRF) in a Bruker S4 Pioneer spectrophotometer.

165   Granulometric distribution of the powdered materials dispersed in distilled water was

166   obtained using a Malvern Mastersizer 2000 laser diffraction instrument while the Z

167   potential measurements were carried out in a DLS Malvern Zetasizer Nano-ZS device.

168   The viscosity of the slurries was measured by means of a concentric cylinder viscometer

169   from Brookfield model DV-II+. Textural characterization (BET specific surface area and

170   pore volume measurements) was carried out over pre-evacuated at 200 ºC (2 h) samples

171   in a Quantachrome Autosorb IQ equipment. X-ray diffraction (XRD) diagrams were

172   recorded for powdered samples employing a Bruker diffractometer and Cu Kα radiation.

173   XRD data were processed using the Powder Cell 2.4 software in order to estimate phases

174   percentages and average crystallite sizes. The catalysts were also studied by scanning

175   electron microscopy (SEM), obtaining both images and Energy-dispersive X-ray (EDX)

176   compositional analysis spectra in a FEG Nova NanoSEM 450 microscope operating at 30

177   kV. In addition, both H_2 and O_2 chemisorption volumetric isotherms were obtained at 50

178   ºC for samples which had been previously reduced with $H_2(5\%)$/Ar at 600 ºC (2 h) and

179   evacuated at 600 ºC (1 h). For these experiments, the adsorbed volumes were determined

180   by extrapolation of the linear part of the adsorption isotherms (in the 100-300 Torr range)

181   to zero pressure, and a chemisorption stoichiometry ratio of 1:1 was assumed for both

182   molecule probes, H:Ni and O:Ni. Temperature-Programmed Reduction (TPR) diagrams

183   and reaction profiles at programmed temperature were recorded in an Autochem II 2920

184   equipped with thermal conductivity detector (TCD) and a Pfeiffer QSM-200 mass

185   spectrometer, respectively.

186   Sample preparation for STEM observation was carried out in a Zeiss Auriga FIB-

187   SEM system operating at 30 keV (ion beam) and equipped with an Omniprobe

188   micromanipulator, which allows an in-situ lift-out of the electron-transparent lamellas.

189   Previous to the FIB preparation, the sample was covered by sputtering (ex situ) with a

190   thin layer (<10 nm) of Au to avoid as much as possible charge effects during the

191   preparation process. A protective layer (in this case, platinum layer: $20 \times 2 \times 2$ μm) was

192 placed in situ via ion induced deposition on the specific region of interest in order to avoid

193 severe damage on the surface. STEM studies, both in High Angle-Annular Dark-Field

194 (HAADF) and analytical EDX modes were performed in an aberration-corrected FEI

195 Titan[3] Themis 60-300 microscope operating at 200 kV. A condenser aperture of 50 μm

196 and a 91 mm camera length was used, obtaining an electron probe with a convergence

197 angle of 20 mrad. In order to get a high signal-to-noise ratio, a beam current of 0.2 nA

198 was used. The EDX hypermaps were recorded using a Super-X EDX system, which

199 gathers the signals from 4 window-less EDX detectors surrounding the TEM sample and

200 provides collection of the signals from a solid angle close to 1 srad.

201 *2.4.   Catalytic tests*

202 Catalytic performance in the DRM reaction was evaluated for both powdered and

203 honeycomb monolithic samples. These tests were run in quartz reactors, at atmospheric

204 pressure and using a 1:1 mixture of pure CH_4 and CO_2 as feedstock. For powders, 26 mg

205 of sample were diluted in 52 mg of SiC, adjusting the total flow to 50 mL min^{-1}. In the

206 case of monoliths, we employed 21 mm long pieces, containing 13 mg of catalyst, and a

207 total flow of 25, 50 or 75 mL min^{-1} depending on the WHSV selected. Small pieces of

208 quartz at the inlet were included to guarantee a turbulent flow. The investigated range of

209 WHSV, expressed as the ratio between reactants flow and sample amount, was 115-346

210 L $g^{-1} h^{-1}$, while Time on Stream (TOS) in these experiments varied from 24 to 48 h. In all

211 cases the catalysts were subjected to a reduction pre-treatment with 60 mL min^{-1} of

212 $H_2(5\%)$/Ar at 600 ℃ (2 h). The reaction temperature was measured by means of a

213 thermocouple located in contact with the quartz reactor at the position of the catalytic

214 bed. The gas analysis at the inlet and outlet of the reactor was performed by gas

215 chromatography (Bruker 450-GC), using helium (25 mL min^{-1}) as carrier inert gas.

216   Reactants (CH_4 and CO_2) conversion values were calculated from the inlet and outlet

217   molar fractions of the individual gases as follows:

218
$$CH_4 \text{ Conversion (\%)} = 100 \times \frac{[CH_4]_{inlet} - [CH_4]_{outlet}}{[CH_4]_{inlet}}$$

219
$$CO_2 \text{ Conversion (\%)} = 100 \times \frac{[CO_2]_{inlet} - [CO_2]_{outlet}}{[CO_2]_{inlet}}$$

220   The estimate of thermodynamic conversion limit values was performed using the

221   DETCHEM software [31].

222   A complementary study aimed to establishing the temperature range of the above

223   commented catalytic tests were done by means of Temperature-Programmed Reaction

224   experiments, heating (5 ℃ min^{-1}) the samples under a flow of CH_4(20%)/CO_2(20%)/He

225   and using mass spectrometry as analytical tool.

226

3. Results and discussion

3.1. Characterization and properties of the powdered samples

229   The Ce/Zr molar ratio in the CZ sample and the nickel content in the NiCZ

230   powdered catalyst (Table 1) were close to the nominal values. The nickel content of the

231   powdered catalyst proportionally decreased in the NiCZ-S sample due to mixing with the

232   alumina used as additive to prepare stable slurries of the active phases prior to the

233   cordierite coating. This alumina is also responsible of the increase of BET specific surface

234   area and pore volume observed for both the support and the catalyst (illustrated in Table

235   1 as well).

236

237

238

239   **Table 1.** Physico-chemical properties of the powdered samples as measured by means of ICP-AES, N_2
240   physisorption and volumetric chemisorption**.**

	CZ	CZ-S	NiCZ	NiCZ-S
Ce/Zr (molar ratio)	0.18	0.18	0.18	0.18
Ni (wt%)	n.a.	n.a.	4.5	3.9
S_{BET} ($m^2 g^{-1}$)	13.3	23.0	15.6	20.7
V_p ($cm^3 g^{-1}$)	0.051	0.074	0.048	0.064
H_2 adsorption ($\mu mol\ g^{-1}$) [a]	-	-	21.9	7.0
O_2 adsorption ($mmol\ g^{-1}$) [a]	0.216	0.221	0.227	0.238

241   [a] Data obtained for samples activated with H_2(5%)/Ar at 600 ºC.

242

243   It is worth mentioning that all studied samples were mesoporous, as denoted by

244 both the N_2 adsorption-desorption isotherms and the derived pore size distribution curves

245 (Fig. 1). In all cases the isotherms were of type IV with a H1 hysteresis loop, usually

246 associated with porous materials that consist of agglomerates or compacts of

247 approximately uniform spheres in fairly regular array, and hence having relatively narrow

248 pore size distributions [32]. On the other hand, the pore size distribution curves show that,

249 as expected, incorporating nickel to the CZ support induces the disappearance of some

250 pores, especially those above 10 nm in diameter, most likely due to partial blocking by

251 the nanostructures comprising this metal component. A similar effect is observed when

252 comparing the curves of CZ-S and NiCZ-S, as it was also previously reported for other

253 supported metal catalysts [30,33]. In contrast, the increase of porosity due to the addition

254 of alumina, as commented above, becomes evident when comparing the curves of the CZ

255 - CZ-S or NiCZ - NiCZ-S counterparts.
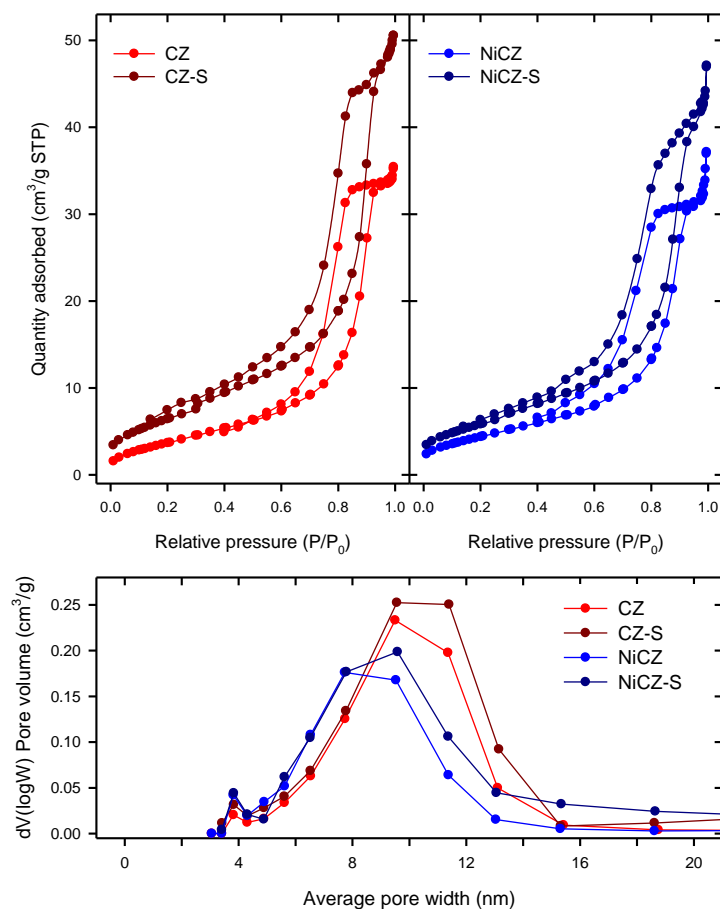
Fig. 1. N_2 physisorption isotherms (upper part) obtained for the powdered supports and catalysts samples of this study. The full and empty symbols correspond to adsorption and desorption branches respectively. Pore size distribution curves obtained from the N_2 physisorption experiments are included below.

Fig. 2 illustrates the effect on the structure of incorporating cerium onto the commercial zirconium oxide and applying the SRMO treatment proposed in [29] to improve the redox performance of the catalytic support, according to XRD. For comparison, the diffractograms of a pure ZrO_2 sample both fresh and after the same SRMO treatment are also included. The starting zirconia (36% monoclinic and 64% tetragonal) suffers the martensitic tetragonal-to-monoclinic phase transformation [34] when the SRMO is applied, rendering a 91% monoclinic and 9% tetragonal material. The presence of cerium favors the cubic/tetragonal phases [35] and indeed our CZ sample contains only 10% monoclinic (JCPDS 37-1484), 5% cubic (JCPDS 27-0997) and 85%

12

270   tetragonal (JCPDS 80-0965) zirconia phases. The absence of peaks related to pure ceria

271   and the presence of shoulders located around 29.5º, 49.4º and 58.3º besides the main

272   diffraction peaks suggests the formation of a ceria-zirconia solid solution that can be

273   related with a tetragonal phase referred to as $Ce_{0.18}Zr_{0.82}O_2$ (JCPDS 80-0785).

274   In the case of the nickel catalyst, relatively low intense peaks, which can be

275   attributed to the (200) and (111) planes of monoclinic nickel oxide (JCPDS 65-6920),

276   were additionally detected. The NiO crystal size estimated by the Debye-Scherrer formula

277   was 17 nm and 15 nm for the NiCZ and NiCZ-S samples, respectively. Regarding the

278   samples containing alumina, practically overlapping XRD diagrams were recorded when

279   comparing CZ with CZ-S, and NiCZ with NiCZ-S, respectively. These results showed

280   that the massive structural nature of the materials is not modified in the suspension used

281   for the preparation of the monolithic catalysts.

282
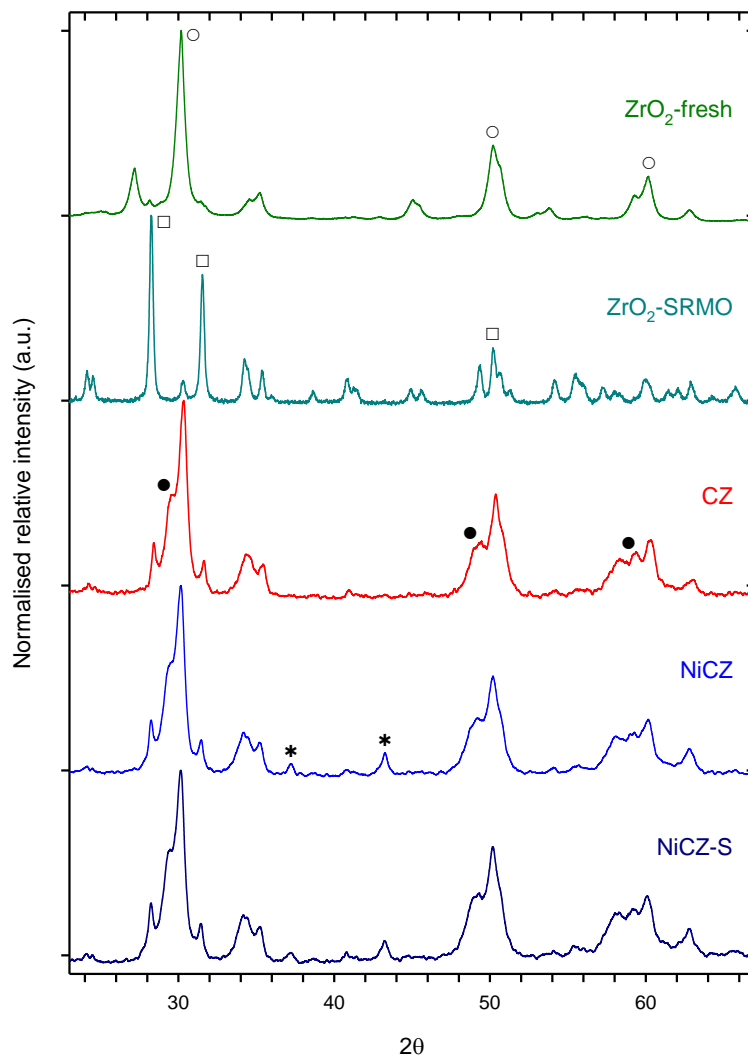
Fig. 2. XRD diagrams obtained from the powdered samples including the zirconia used in this study as
received and submitted to the ageing treatment employed in the case of ceria-containing samples. Main
diffraction peaks corresponding to monoclinic JCPDS 37-1484 (□) and tetragonal JCPDS 80-0965 (○)
zirconia; tetragonal $Ce_{0.18}Zr_{0.82}O_2$ JCPDS 80-0785 (●); and monoclinic NiO JCPDS 65-6920 (✱), are
indicated.

The TPR results (Fig. 3) indicated that cerium reduction in CZ sample starts at
250 ºC, reaching maxima at 480 and 520 ºC resulting from a non-symmetric and broad
profile. Considering that temperature maxima around 600 ºC are reported for the main
reduction peaks in similar Ce-poor/Zr-rich mixed oxides [36], these results probe the
effectiveness of the SRMO pretreatment aging protocol [29] for the oxide support that we
have employed. The NiCZ profile (Fig. 3) is quite complex as shows an intense maximum

14

295 at 325 ºC and shoulders located around 175, 260, 290 and 360 ºC, with a very low but

296 continuous hydrogen consumption up to 750 ºC. The quantitative analysis from the

297 signals (also included in Fig. 3) is consistent with the reduction towards Ce(III) and Ni(0)

298 of the cerium and nickel total amounts for all the samples, considering their initial state

299 in the form of Ce(IV) and Ni(II).
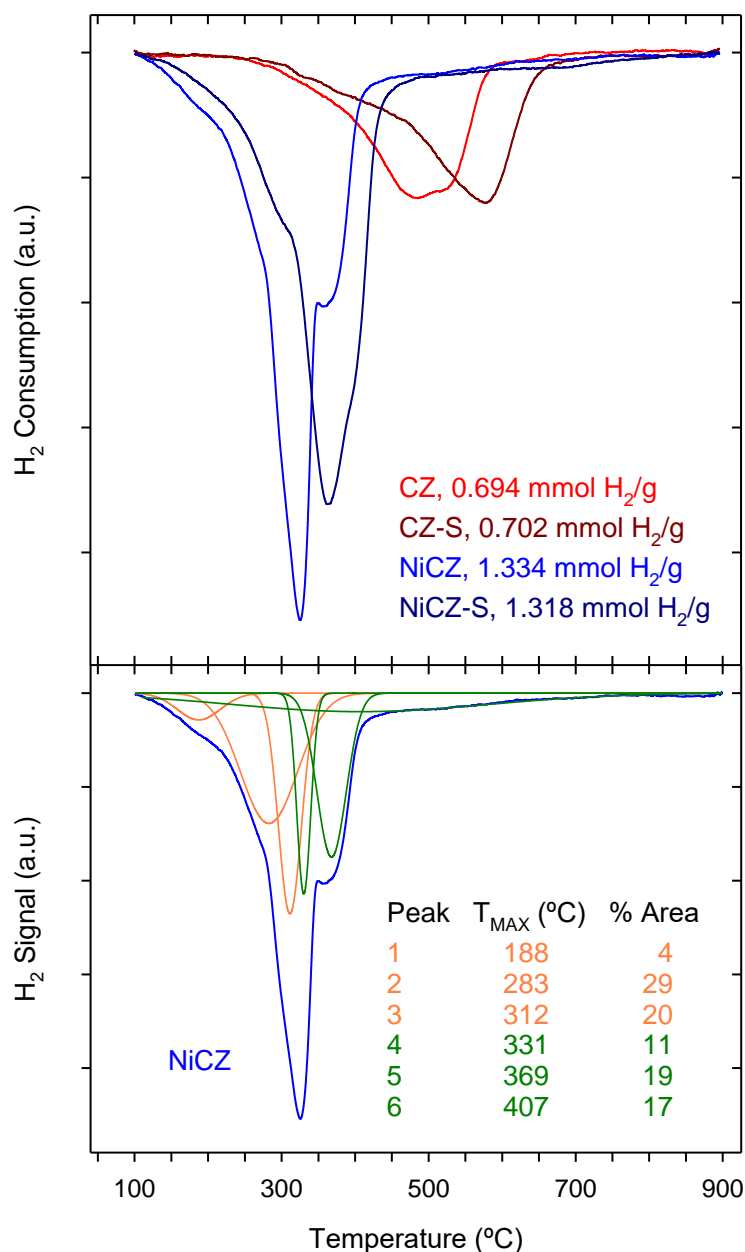
300

301 **Fig. 3.** TPR profiles of the powdered samples under $H_2(5\%)$Ar and a heating rate of 10 ºC min^{-1},

302 including quantitative data (above) and deconvoluted patterns with the position of maxima and area

303 percentages (below) for the NiCZ sample.

304

15

305   The detailed interpretation of TPR profiles of nickel supported on ceria-zirconia

306   binary oxides is difficult [36] as far as there is no agreement in literature regarding the

307   ascription of their features. TPR peaks occurring from 150 ºC and with maxima in the

308   250-400 ºC temperature range have been reported by using deconvolution procedures

309   [9,36], and the differences in temperature for the reduction of supported NiO have been

310   explained in terms of different distribution of particle sizes and/or degrees of interaction

311   with the support [37,38]. On the other hand, reduction of the support and the nickel

312   species can occur simultaneously, promoted by spillover of hydrogen species [9,39], thus

313   significantly lowering the temperature at which the ceria-zirconia solid solution is

314   reduced. Taking into account the quantitative data, and applying the data treatment

315   previously reported [9,36], we can tentatively attribute the first part of the TPR patterns

316   in the NiCZ sample (namely, that fitted by the first three peaks) to the reduction of nickel

317   species, and the remaining high temperature part to the reduction of the support (Fig. 3).

318   Indeed, the hydrogen consumption corresponding to the first three peaks in the

319   deconvoluted patterns for the NiCZ sample (0.707 mmol H_2/g) is close to that

320   theoretically required for complete reduction of nickel from Ni(II) to Ni(0) (0.767 mmol

321   H_2/g). On the other hand, the hydrogen consumption corresponding to the last three peaks

322   (0.627 mmol H_2/g) fits well to that theoretically required for the reduction of cerium from

323   Ce(IV) to Ce(III) (0.644 mmol H_2/g). In the case of the CZ-S and NiCZ-S alumina-

324   containing samples, which are the best references of the phases deposited on the

325   monolithic catalysts, the recorded TPR curves suggest some chemical interaction between

326   the nickel and the support oxide with the alumina; this can be inferred from the shift of

327   the maxima of the reduction peaks towards higher temperatures with respect to the CZ

328   and NiCZ samples (580 ºC and 365 ºC for CZ-S and NiCZ-S, respectively). This is in

329   good agreement with previous reports evidencing that the presence of alumina in nickel

330   supported onto ceria-zirconia mixed oxides shifts to higher temperatures the reduction of

331   both NiO [40,41] and ceria-containing phases [42,43].

332   The results commented above allowed selecting 600 ºC as the catalysts activation

333   temperature in this study, as far as this temperature guaranties that the entire nickel and

334   most of the cerium contained in the samples should be in a reduced form. Previous studies

335   also indicated the need of reducing supported nickel catalysts at relatively high

336   temperatures ($> 550\,ºC$) to guarantee total reduction of this metal [44], a prerequisite well-

337   stablished for obtaining the better catalytic results in DRM [45,46].

338   The nickel catalysts, activated at 600 ºC, chemisorbed a very low amount of

339   hydrogen (Table 1), rendering H/Ni ratios of 0.06 and 0.02 for the NiCZ and NiCZ-S

340   samples, respectively. Similar results, that could be interpreted as evidences of very low

341   nickel dispersion, have been related instead to the existence of strong metal-support

342   interaction (SMSI) that hinders the hydrogen adsorption in ceria-zirconia supported Ni

343   catalysts when submitted to reduction treatments at 600 ºC [7]. In fact, this effect was

344   early reported for nickel catalysts supported onto alumina, silica and titania [47]. The use

345   of O_2 as molecule probe, as proposed in [48], can provide adequate nickel dispersion

346   values when the oxygen consumption from the support is taken as reference (Table 1).

347   The resulting Ni dispersion percentages were 6 (O/Ni = 0.06) and 10 (O/Ni = 0.10) for

348   NiCZ and NiCZ-S catalysts, respectively. The use of the relationship that correlates the

349   average nickel particle size and the metal dispersion in nickel supported catalyst [47]

350   renders 17 and 10 nm for NiCZ and NiCZ-S samples, respectively, in reasonable

351   agreement with the results estimated from XRD line broadening once the structural

352   correction from the reduction of NiO to Ni phases is applied (14 and 13 nm for NiCZ and

353   NiCZ-S, respectively).

354   *3.2. Honeycomb catalysts characterization*

As indicated in the experimental section, the NiCZ was deposited over cordierite honeycombs by washcoating, obtaining relatively low catalysts loadings: 0.33, 0.36, 0.41 and 0.38 mg cm^{-2} for H230CZ, H230NiCZ, H400CZ and H400NiCZ samples, respectively. It should be highlighted that these values are at least one order of magnitude higher in conventional monoliths [49]. The adherence of the coatings was evaluated from the washcoating material weight that remained attached to the cordierite after the ultrasound treatment test, resulting 91, 92, 97 and 95% for H230CZ, H230NiCZ, H400CZ and H400NiCZ samples, respectively. These values are acceptable considering that a maximum weight loss limit of 10% has been obtained for oxide phases-washcoated cordierite honeycomb monoliths under optimum conditions [50]. It is also remarkable that these parameters were not reported in the few previous works dealing with honeycomb-type catalysts for DRM [15,16,18,19], except one in which a cordierite honeycomb was washcoated with a Rh/γ-Al$_2$O$_3$ [17], but the authors did not provide the adherence of the coating and its loading was much higher (43.8 mg cm^{-2}).

The use of SEM with EDX compositional analysis at the micron scale allowed detecting the phase deposited over the cordierite walls. For illustrative purposes, Fig. 4A shows a wall region of the H230NiCZ monolith, with an area of 150 x 125 μm^2, in which the presence of Ni, Ce and Zr is clearly observed. Note how the particles of the catalyst are scattered over the surface of the monolith walls, in a situation far from that corresponding to a continuous film. Likewise, X-ray micro-fluorescence data (Fig. 4B) evidenced a partial coating of the cordierite walls by the active phase in massive state, in good agreement with both the low load of the prepared honeycomb monolithic catalysts and the EDX maps just commented. Moreover, both techniques suggest an appropriate Ni-Ce-Zr interaction in the zones where the deposits of catalyst are found, since the signals of the three elements are present at the same or nearby locations.

380

381
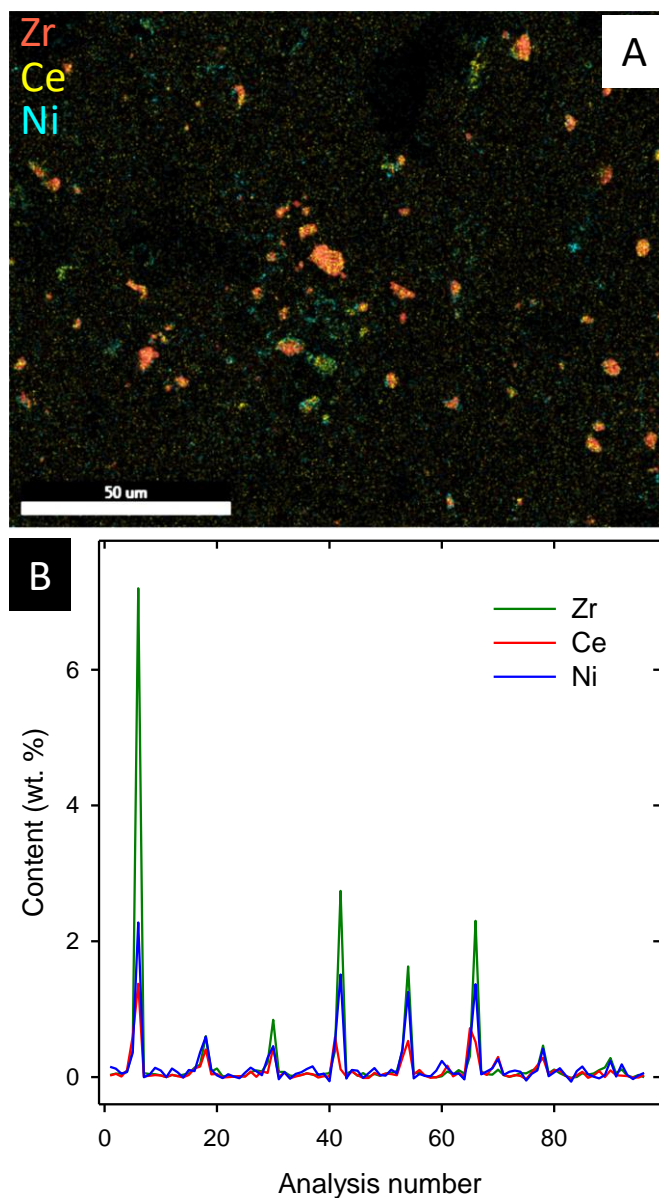
Fig. 4. SEM-EDX compositional mapping (A) and micro-XRF analysis (B) representative of the walls

surface of the H230NiCZ catalyst.

384

An electron-transparent cross section of the outer part of the catalyst coating layer,

Fig. 5, was cut out by FIB using the standard lift-out technique to investigate in more

detail, at the nanometer scale, structural and compositional features of the washcoated

layer by TEM/STEM techniques [26]. Fig. 5A shows a HAADF-STEM image from the

FIB-lamella: the brightest areas observed at the upper part of the image correspond to the

390   Au and Pt protective layers, intentionally sputtered over the sample during different steps

391   of the cross-section preparation by FIB [51]. A more detailed high-magnification image,

392   Fig. 5B, of the upper part of the lamella provided more information about the coating

393   layer.
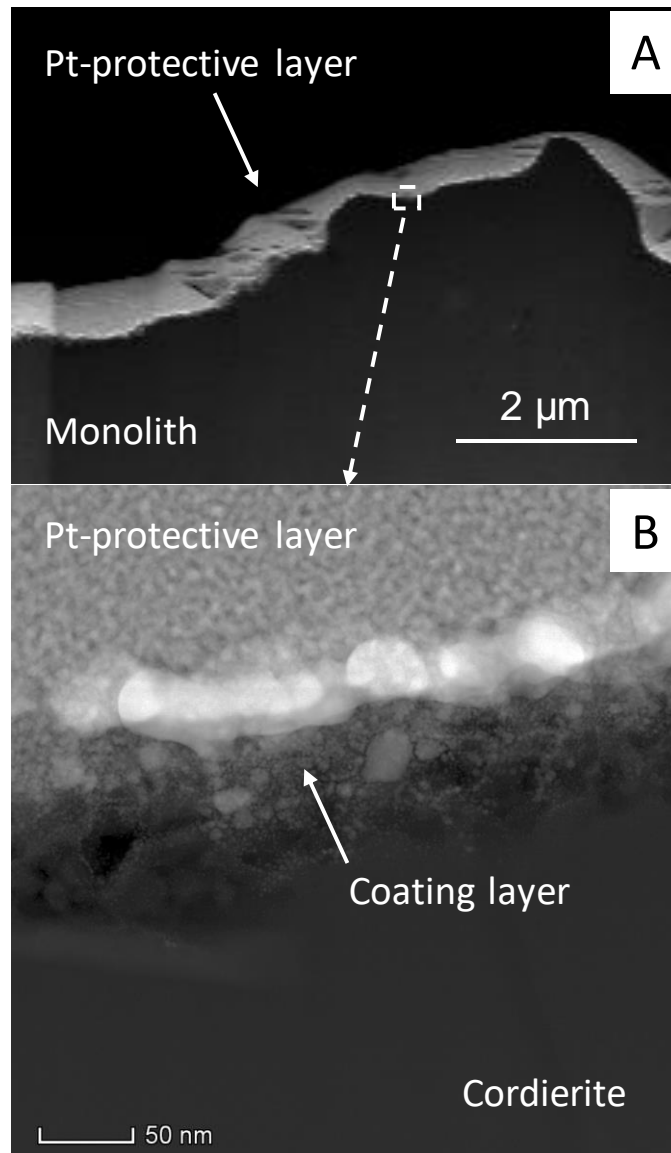
394

395

396   **Fig. 5.** HAADF-STEM images from the H230-NiCZ lamella prepared by FIB at low-magnification (A)
397   and higher magnification image from a selected area (B) revealing the interphase between the coating
398   layer and the cordierite substrate.

399

400   In this sense, three different regions can be clearly identified: from the bottom of

401   the image, a highly dense component depicting homogeneous contrast which corresponds

402   to the cordierite substrate, then a second region which seems grainier, that corresponds to

403   the coating layer, and finally, the upper part belonging to the Pt-protective layer with the

404   Au-film sputtered-layer made during the FIB-lamella preparation. From these images, it

405   can be concluded that the coating layer thickness seems to be notably thin, just tens of

406   nanometers ($\approx$ 50 nm). It is remarkable that this nanometric thick washcoat is orders of

407   magnitude thinner than those commonly found in conventional preparations of monoliths

408   [30]. In any case, from the intensity values of these contrasts, it is not possible to

409   discriminate to which component they correspond to. For this purpose, STEM–EDX is

410   the most adequate tool. Note that STEM–EDX maps acquired with nanometer resolution

411   allow discriminating between these components thanks to the elemental chemical

412   analysis. Fig. 6A shows the corresponding chemical results obtained from the same area

413   highlighted in Fig. 5B. Thus, combining EDX chemical elemental maps, the distribution

414   of the different elements comprising the active phase as well as those of the cordierite

415   substrate are now clearly visualized. Comparing the different maps, it seems clear that

416   the highly-dense component, depicting homogeneous contrast, at the bottom part of the

417   HAADF-STEM image, corresponds (see Si elemental map) to the cordierite substrate.

418   Note how the surface of the ceramic monolith is not totally flat but presents local

419   roughness at the scale of tens of nanometers. In fact, a crest and valley structure are clearly

420   revealed both in the HAADF-STEM image and in the Si map.

421
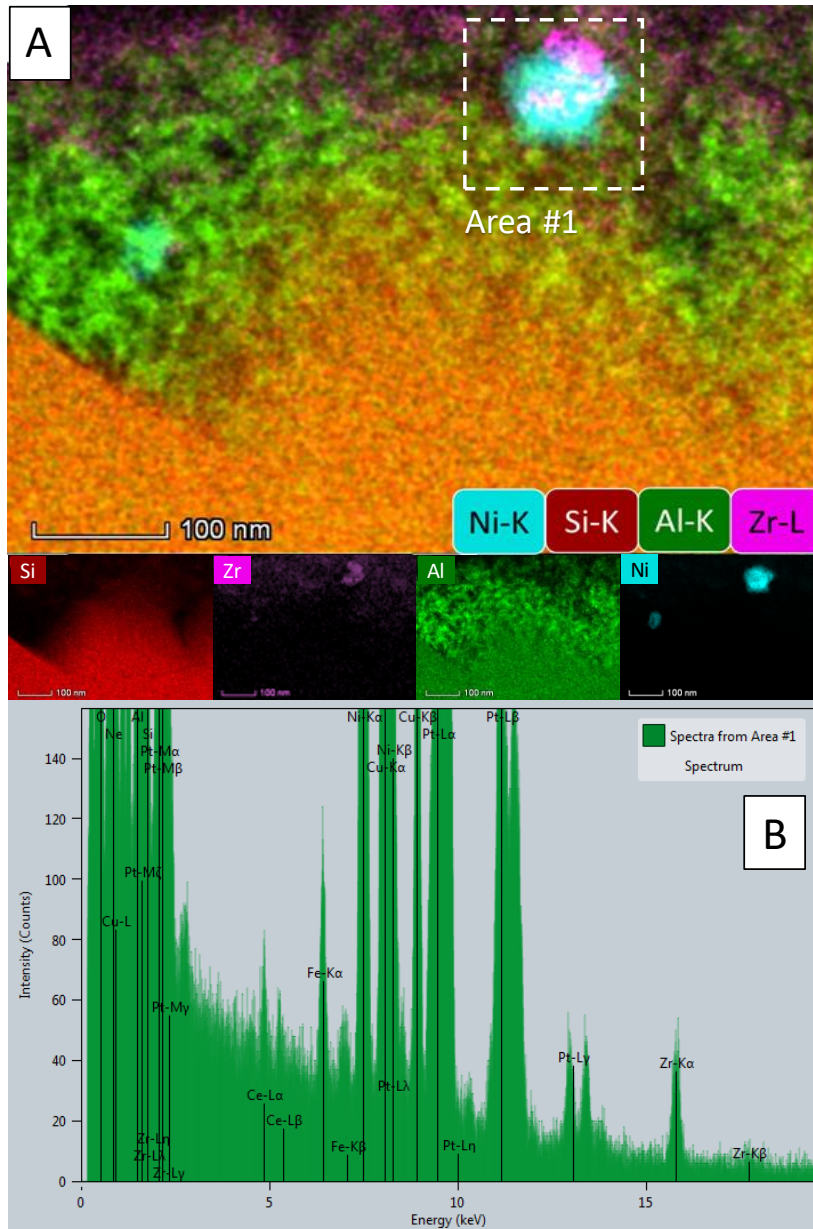
Fig. 6. (A) Composed EDX map illustrating the distribution of the different elements from active phase and cordierite substrate. Individual EDX elemental maps for Ni, Al, Si and Zr, respectively are shown below. (B) EDX spectrum from a selected area, labelled as Area#1. All data correspond to a H230-NiCZ lamella prepared by FIB (Fig. 5).

Regarding the Al elemental map, two different regions are observed. One less dense at the top, depicting a grainy aspect, with nanometer-sized pores, where no signal from Si is observed; and a more compact one at the bottom extending over the same area of the Si map. These two different density areas are related with different components.

432 Thus, the grainier region is assigned to Al_2O_3 from the coating layer, since no-Si signal

433 is detected, and the compact one to the cordierite substrate. Note how the coating layer

434 fills perfectly the valleys on the cordierite surface in a continuous fashion, which points

435 outs a successful wetting of the monolith during the washcoating step. Moreover, the

436 coating layer is directly demonstrated to be highly porous, in cross-section, which is

437 undoubtedly a key issue in terms of accessibility of reactants to the active catalyst

438 component.

439 Lastly, the location of the active phase elements is evidenced by the presence of

440 Ni and Zr signals, respectively. The maps clearly show that Ni nanoparticles are in close

441 contact with Zr-particles. The map corresponding to Ce is not shown in Fig. 6 considering

442 that this lanthanide generates very weak-signals in the EDX experiments, see Fig. 6B,

443 and its elemental maps are much noisier than those of Zr and/or Ni elements. In addition,

444 any elemental quantification should be taken with caution as the analyzed area

445 corresponds to a tiny portion of the washcoat.

446 Summarizing, the combination of the HAADF-STEM images and the STEM–

447 EDX results have allowed identifying the catalytic active phase nanoparticles in micron-

448 size areas of the coating of our monolithic devices. This suggests that not only the coating

449 layer is extremely thin and porous but also that the active phase is highly spread over the

450 monolith, which is in good agreement with SEM and XRF data as well as with the low

451 loading measured for the devices.

452 3.3 *Catalytic performance*

453 In order to establish the operating conditions in the DRM reaction for our

454 catalysts, semi-quantitative Temperature-Programmed Reaction profiles of the evolution

455 of CO_2, CH_4, CO, H_2 and H_2O by means of mass spectrometry were recorded (Fig. 7).

456
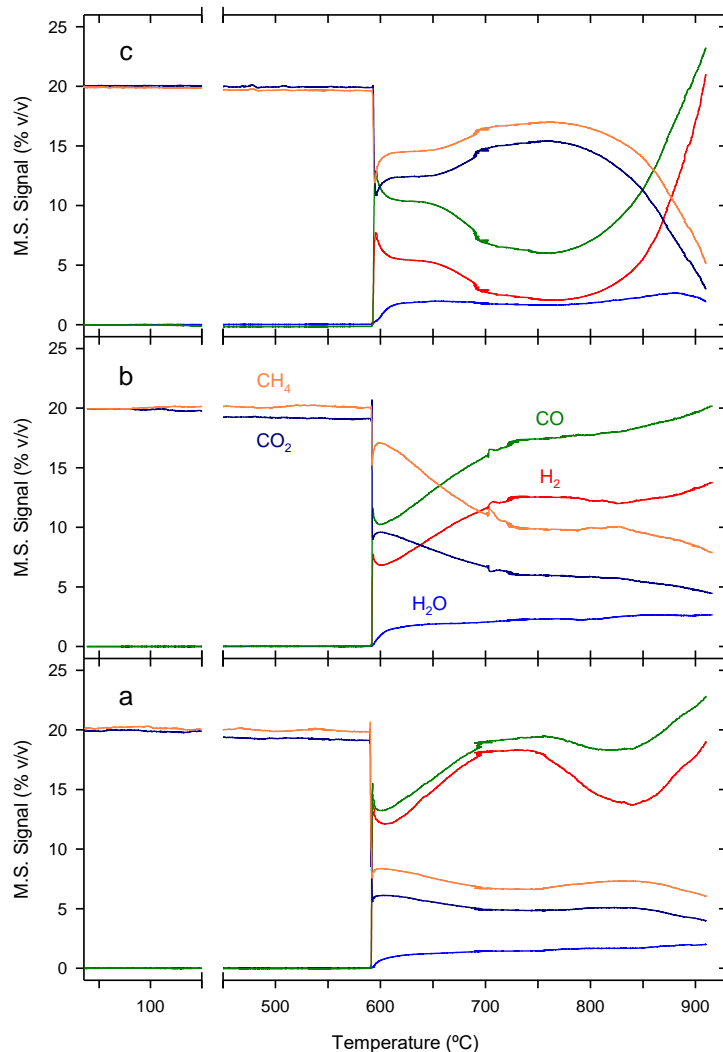
Fig. 7. Evolution with temperature of the indicated species for NiCZ (a), NiCZ-S (b) and H230NiCZ (c) samples submitted to heating (5 ℃ min^{-1}) under CH_4(20%)/CO_2(20%)/He, as recorded by mass spectrometry.

For all the studied samples the reaction abruptly activates around 600 ℃, temperature at which CH_4 and CO_2 consumption along with CO and H_2 production are detected. From that point on, the evolution with temperature of the outlet gas composition is different for the NiCZ, NiCZ-S and H230NiCZ samples. As far as the DRM process occurs in parallel and simultaneously with several secondary reactions [52], the detailed analysis of these results becomes complex, in particular because the continuous increase

24

469 in temperature leads to a non-stationary regime for this type of experiments. Nevertheless,

470 in all the samples, H_2O formation was detected throughout the whole temperature range

471 where catalytic activity is observed, what indicates that the Reverse Water Gas Shift

472 (RWGS) reaction occurs in parallel with DRM. In fact, CO_2 conversion values were

473 always higher than those of CH_4, and the H_2/CO ratios in the outlet gas were lower than

474 1. According to the recorded profiles, the temperature range from 700 ℃ to 900 ℃ would

475 be the most appropriate in relation to the conversion values reached. In this sense, it is

476 important to point out that Wang et al. [53] reported a maximum in the carbon production,

477 caused by CH_4 decomposition or the Boudouard reaction, in the temperature range 557

478 to 700 °C. On the other hand, and also from thermodynamic considerations, temperatures

479 around 900 ℃ have been suggested as optima when a $CO_2/CH_4 = 1:1$ feed ratio is

480 employed, since it allows a balance between the conversion achieved and the carbon

481 formation phenomena [5].

482   Table 2 summarizes the most significant results obtained in the quantitative

483 evaluation of the catalytic activity of the prepared samples in the DRM reaction,

484 monitored by means of gas chromatography. In order to meet stringent conditions in terms

485 of stability, conversion data for CO_2 and CH_4 along with H_2/CO ratio values after times

486 on stream (TOS) equal or superior to 24 h were measured. As it can be seen, under the

487 studied experimental conditions, even at the highest temperature (900 ℃) the cordierite

488 used as monolithic support is inactive, while the CZ-S sample shows reactant conversions

489 not higher than 10%, similar to those obtained for the H230CZ monolith sample. On the

490 contrary, both honeycomb monolithic catalysts, H230NiCZ and H400NiCZ, exhibit a

491 significant activity in the 700-900 ℃ range, the reactant conversion increasing with

492 temperature. As we emphasized in our preliminary study [28], it should be highlighted

493 that this remarkable performance at all temperatures and WHSV values is obtained with

494 monoliths containing a very small specific loading of the washcoat (<0.40 mg cm^{-2}), a

495 value at least one order of magnitude lower than in conventional monoliths [49].

496

497   **Table 2.** Catalytic performance in the DRM reaction using a 1:1 CO_2:CH_4 mixture and after 24 h.

Sample	WHSV (L g^{-1} h^{-1})	T (ºC)	CO_2 Conv. (%)	CH_4 Conv. (%)	H_2/CO ratio
CZ-S	115	900	10	8	0.15
NiCZ	115	750	20	11	0.25
NiCZ	115	900	95	92	0.89
NiCZ-S	115	750	36	22	0.50
NiCZ-S	115	900	84	78	0.82
H230 [a]	n.a.	900	3	0	-
H230CZ	115	900	13	14	0.93
H230NiCZ	115	700	84	77	0.79
H400NiCZ	115	700	81	73	0.78
H230NiCZ [b]	115	750	93	89	0.85
H400NiCZ [c]	115	750	89	83	0.83
H230NiCZ [c]	231	750	94	90	0.86
H230NiCZ	346	750	90	85	0.85
H230NiCZ	115	800	93	89	0.88
H400NiCZ	115	800	96	93	0.90
H230NiCZ	115	900	96	94	0.89
H400NiCZ	115	900	99	98	0.94

498   [a] Data obtained for a complete piece of cordierite; [b] Data after 43 h of reaction; [c] Data after 48 h of
499   reaction.

500

501   For these nickel-containing monoliths samples, in the whole temperature interval

502 under study, the CO_2 conversion keeps higher while the CH_4 conversion is lower than

26

503   thermodynamic limit values calculated from a direct minimization of Gibbs free energy

504   method using Aspen Plus software [54]. Data reported from these authors (Table 3)

505   consider an equilibrium analysis of a complex multi-reaction system for carbon dioxide

506   reforming of methane in parallel with a significant carbon formation. On the contrary, our

507   results suggest a relatively higher contribution of the RWGS reaction and a less intense

508   methane cracking process when DRM is conducted onto the here proposed monolithic

509   catalysts. Indeed, the calculated thermodynamic conversion for both reactants is closer to

510   the experimental data when the reaction system is modelled minimizing the carbon

511   formation processes (Table 3).

512

513   **Table 3.** CO_2 and CH_4 equilibrium conversion data for the DRM reaction conducted at 1 atm and with
514    $CH_4:CO_2 = 1:1$ based on thermodynamic analysis

Temperature (ºC)	CH_4 Eq. Conv. (%)[a]	CH_4 Eq. Conv. (%)[b]	CO_2 Eq. Conv. (%)[a]	CO_2 Eq. Conv. (%)[b]
700	92	84	65	91
750	94	91	78	94
800	96	95	88	97
900	98	98	96	99

515   [a] Analysis reported in [33] based on direct minimization of Gibbs free energy method using Aspen plus
516   sotfware. [b] Data obtained in this work for a reaction system in which the carbon formation processes are
517   minimized using DETCHEM software.

518

519   It is noteworthy that both the H230NiCZ and H400NiCZ catalysts present

520   significantly higher conversions than the reference NiCZ and NiCZ-S powders at 750 ºC

521   and 115 L g^{-1} h^{-1}, this suggesting that the honeycomb monolithic design (no matter the

522   cell density) prevents from the kinetic control that operates in powdered samples under

the highly demanding WHSV regime here employed [55]. This comparison between

monolith and powders is also favorable to the first if the activity is expressed as CH_4

consumed per unit of time and Ni mass. For example, under the above experimental

conditions, we have obtained values of 13.0, 3.2 and 1.6 mmol CH_4 s^{-1} g^{-1} Ni, for the

H230NiCZ, NiCZ-S and NiCZ samples, respectively, for the TOS values indicated in

Table 2. Moreover, it is necessary to increase the temperature of the powdered catalysts

up to 900 ºC in order to obtain a catalytic performance similar to that of the monolithic

catalysts. Also remarkable, the advantage of the monolithic catalysts remains even at very

high flow/catalyst amount ratios, WHSV=346 L g^{-1} h^{-1} (Table 2), unusual experimental

conditions scarcely explored in literature [5,25]. In the same way, it is noticeable that our

catalysts are very competitive when compared with powdered nickel catalysts onto

optimized supports, such as $Ni/CeYZrO_x$ [9], as well as other powdered $Ni/MgO-ZrO_2$

catalysts which contain promoters (Co, Ca, K, Ba, La, Ce) [56], or even with noble metals

such as supported Pt or Ru [25]. Moreover, our results are also better when compared

with the scarce references that employed Ni catalysts supported onto honeycomb

monoliths, either of cordierite [16] or metallic [19]. Furthermore, as mentioned in the

introduction section, in the cited references nickel was promoted by small amounts of Ru

and Pd-Sn, respectively. Only in [15] some of the samples exhibited superior

performance, but the authors employed higher amounts of nickel (11 wt%), which was

also doped with alkali and rare-earth metal oxides.

The H_2/CO ratio is also an important output in DRM reaction, values close to 1

being desired to allow an easier adaptation to many downstream processes including

ammonia and methanol synthesis [25] and Fischer-Tropsch synthesis [6]. On this regard,

we obtained H_2/CO ratio data ranging from 0.78 up to 0.94 for all the studied nickel-

containing honeycomb samples.

548   Finally, regarding stability under reaction conditions, Fig. 8 shows some reaction

549   profiles versus time selected from the whole series of tested catalysts.

550
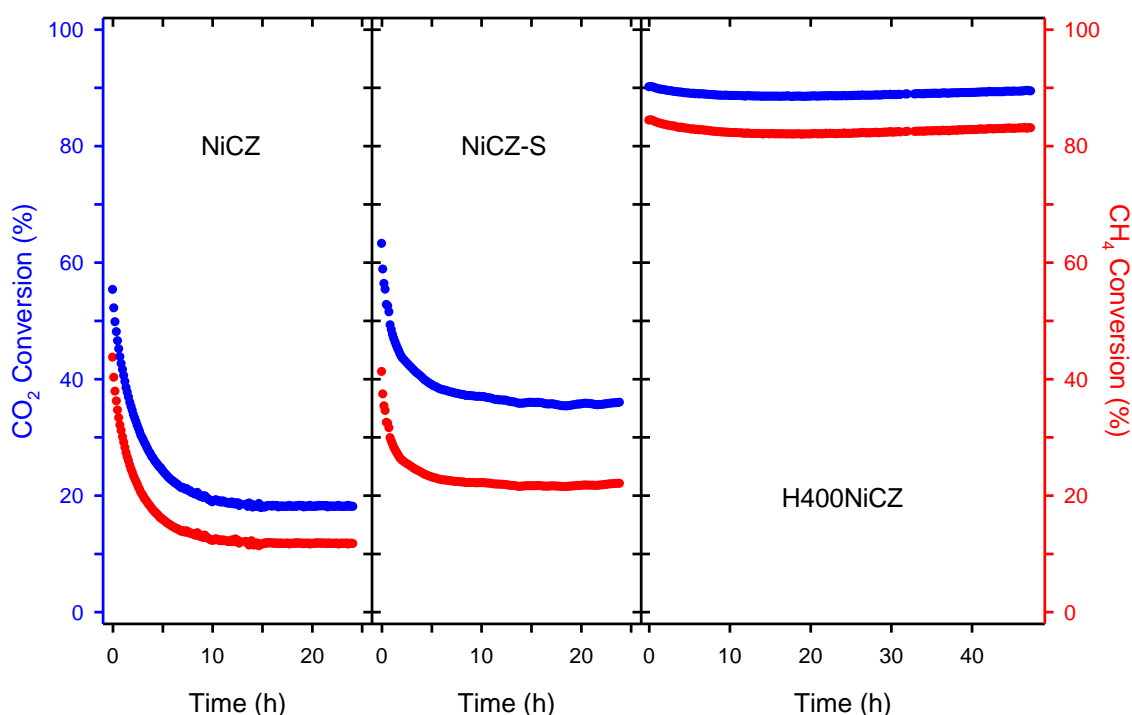
Fig. 8. Evolution with TOS of the reactants conversion in the DRM reaction for the catalysts indicated operating at 750 ℃ with $CH_4:CO_2 = 1:1$ and WHSV = 115 L g^{-1} h^{-1}.

553

554   Note first that in the case of both powdered catalysts, a clear deactivation

555   phenomenon at 750 ℃ is observed, with approx. 70% and 40 % for NiCZ and NiCZ-S,

556   respectively, of conversion decrease after 24 h of TOS. Moreover, this effect is relatively

557   fast being more intense during the first 5 hours. The slightly lower decay in the NiCZ-S

558   sample should be related to the positive effect of alumina on the texture, nickel dispersion

559   and the interaction between the catalyst components above discussed in the

560   characterization results. This interpretation is also supported by literature which

561   demonstrates that a smaller nickel crystal size could retard coking [6,57] while the active

562   phase-alumina interaction might favor resistance against sintering [58,59]. It is

563   particularly remarkable the H400NiCZ catalyst behavior which keeps its high conversion

564   value even after 48 h of reaction time. This result suggests that the honeycomb monolithic

565 design also allows limiting deposition and progressive accumulation of carbon from deep

566 methane cracking reaction [60], which leads to pressure increase in packed beds [54] that

567 in turn may cause flow blockage and even reactor breakup [9]. At this respect, the use of

568 the honeycomb reactor designs could represent a reasonable alternative to conventional

569 catalytic devices or non-conventional technologies recently proposed [61].

570

571 **4. Conclusions**

572   In this work, honeycomb monolithic catalysts of nickel supported on a

573 nanostructured CeO_2/ZrO_2 with enhanced redox performance were prepared by the

574 washcoating method, using cordierite with different cell density (230 and 400 cpsi) but

575 reaching similar catalyst specific loading, and tested in the dry reforming of methane

576 (DRM). For the first time, to the best of our knowledge, nickel supported on ceria-zirconia

577 oxides with advanced redox properties, reached by means of severe reduction plus mild

578 oxidation treatments, were employed after deposition onto a honeycomb-type structured

579 support. Working with pure reactants at a relatively low temperature (750 ºC) and

580 operating with WHSV as high as 346 L g^{-1} h^{-1}, conversion and H_2/CO ratio values close

581 to the thermodynamic limits were reached. Moreover, the catalytic activity kept stable

582 during prolonged experiments of 24-48 h of time-on-stream. These results are particularly

583 noticeable considering that the reference powdered catalyst, studied in parallel, showed

584 poorer catalytic performance, especially for low values of the temperature range studied

585 (750-900 ºC).

586   STEM analysis of an electron-transparent cross-section of the monolith, prepared

587 by FIB, revealed an ultrathin, just tens of nanometers thick, washcoated layer anchored

588 to the rough surface of the cordierite substrate. This layer is made up of a porous alumina

589 network in which the active phase catalyst nanoparticles are highly spread, thus resulting

590   in very low washcoat loading (<0.40 mg cm^{-2}). STEM-EDS analysis also evidenced a

591   thigh contact between nickel, ceria and zirconia in the washcoated layer.

592   The relative low content and dispersion of nickel in the washcoat does not prevent

593   the catalyst from a very high efficiency in the investigated reaction. This finding can be

594   related with the characterization performed which suggested the occurrence of metal-

595   support interactions. This effect, along with the inherent advantages of the honeycomb

596   monolithic design, might explain the high activity and outstanding stability observed in

597   DRM.

598

599   **Author statement**

600   Fazia Agueniou: Investigation; José M. Gatica: Conceptualization & Methodology,

601   Writing - Review & Editing, Supervision; M. Pilar Yeste: Investigation; Juan C.

602   Hernández-Garrido: Investigation; Miguel A. Cauqui: Conceptualization &

603   Methodology, Funding acquisition; José M. Rodríguez-Izquierdo: Resources; José J.

604   Calvino: Conceptualization & Methodology, Funding acquisition; Hilario Vidal:

605   Conceptualization & Methodology, Writing - Original draft preparation, Supervision.

606

607

608 **Declaration of competing interest**

609 The authors declare no competing financial interest.

610

611 **Acknowledgements**

617

618

619 **References**

620 [1] N. Laosiripojana, W. Sutthisripok, S. Assabumrungrat, Synthesis gas production from

621 dry reforming of methane over CeO_2 doped Ni/Al_2O_3: Influence of the doping ceria on

622 the resistance toward carbon formation, Chem. Eng. J. 112 (2005) 13-22.

623 https://doi.org/10.1016/j.cej.2005.06.003

624 [2] B. Abdullah, N.A.A. Ghani, D.N. Vo, Recent advances in dry reforming of methane

625 over Ni-based catalysts, J. Cleaner Prod. 162 (2017) 170-185.

626 http://dx.doi.org/10.1016/j.jclepro.2017.05.176

627   [3] A. Vita, G. Cristiano, C. Italiano, L. Pino, S. Specchia, Syngas production by methane

628   oxy-steam reforming on Me/CeO$_2$ (Me = Rh, Pt, Ni) catalyst lined on cordierite

629   monoliths,   Appl.   Catal.   B   162   (2015)   551-563.

630   http://dx.doi.org/10.1016/j.apcatb.2014.07.028

631   [4] J.W. Han, J.S. Park, M.S. Choi, H. Lee, Uncoupling the size and support effects of Ni

632   catalysts for dry reforming of methane, Appl. Catal. B 203 (2017) 625-632.

633   http://dx.doi.org/10.1016/j.apcatb.2016.10.069

634   [5] W.-J. Jang, J.-O. Shim, H.-M. Kim, S.-Y. Yoo, H.-S. Roh, A review on dry reforming

635   of methane in aspect of catalytic properties, Catal. Today 324 (2019) 15-26.

636   https://doi.org/10.1016/j.cattod.2018.07.032

637   [6] S. Arora, R. Prasad, An overview on dry reforming of methane: strategies to reduce

638   carbonaceous deactivation of catalysts, RSC Adv. 6 (2016) 108668-108688.

639   https://doi.org/10.1039/c6ra20450c

640   [7] A. Wolfbeisser, O. Sophiphun, J. Bernardi, J. Wittayakun, K. Futtinger, G.

641   Rupprechter, Methane dry reforming over ceria-zirconia supported Ni catalysts, Catal.

642   Today 277 (2016) 234-245. http://dx.doi.org/10.1016/j.cattod.2016.04.025

643   [8] M.A. Vasiliades, P. Djinović, L.F. Davlyatova, A. Pintar, A.M. Efstathiou, Origin and

644   reactivity of active and inactive carbon formed during DRM over Ni/Ce$_{0.38}$Zr$_{0.62}$O$_{2-\delta}$

645   studied by transient isotopic techniques, Catal. Today 299 (2018) 201-211.

646   http://dx.doi.org/10.1016/j.cattod.2017.03.057

647   [9] M.A. Muñoz, J.J. Calvino, J.M. Rodríguez-Izquierdo, G. Blanco, D.C. Arias, J.A.

648   Pérez-Omil, J.C. Hernández-Garrido, J.M. González-Leal, M.A. Cauqui, M.P. Yeste,

649 Highly stable ceria-zirconia-yttria supported Ni catalysts for syngas production by CO_2

650 reforming of methane, Appl. Surf. Sci. 426 (2017) 864-873.

651 http://dx.doi.org/10.1016/j.apsusc.2017.07.210

652 [10] N.A.K. Aramouni, J.G. Touma, B.A. Tarboush, J. Zeaiter, M.N. Ahmad, Catalyst

653 design for dry reforming of methane: Analysis review, Renew. Sustain. Energy Rev. 82

654 (2018) 2570-2585. http://dx.doi.org/10.1016/j.rser.2017.09.076

655 [11] M. Mohamedali, A. Henni, H. Ibrahim, Recent advances in supported metal catalysts

656 for syngas production from methane, Chem. Eng. 2(1) (2018) 9.

657 https://doi.org/10.3390/chemengineering2010009

658 [12] Y. Zhan, J. Han, Z. Bao, B. Cao, Y. Li, J. Street, F. Yu, Biogas reforming of carbon

659 dioxide to syngas production over Ni-Mg-Al catalysts, Mol. Catal. 436 (2017) 248-258.

660 http://dx.doi.org/10.1016/j.mcat.2017.04.032

661 [13] S. Aghamohammadi, M. Haghighi, M. Maleki, N. Rahemi, Sequential impregnation

662 vs. sol-gel synthesized Ni/Al_2O_3-CeO_2 nanocatalysts for dry reforming of methane: effect

663 of synthesis method and support promotion, Mol. Catal. 431 (2017) 39-48.

664 http://dx.doi.org/10.1016/j.mcat.2017.01.012

665 [14] S. Sangsong, M. Phongaksorn, S. Tungkamani, T. Sornchamni, R. Chuvaree, Dry

666 methane reforming performance of Ni-based catalyst coated onto stainless steel substrate,

667 Energy Procedia 79 (2015) 137-142. http://dx.doi.org/10.1016/j.egypro.2015.11.450

668 [15] S.O. Soloviev, A.Y. Kapran, S.N. Orlyk, E.V. Gubareni, Carbon dioxide reforming

669 of methane on monolithic Ni/Al_2O_3-based catalysts, J. Nat. Gas Chem. 20 (2011) 184-

670 190. http://dx.doi.org/10.1016/S1003-9953(10)60149-1

671 [16] I. Luisetto, C. Sarno, D. De Felicis, F. Basoli, C. Battocchio, S. Tuti, S. Licoccia, E.

672 di Bartolomeo, Ni supported on- γ-Al_2O_3 promoted by Ru for the dry reforming of

673 methane in packed and monolithic reactors, Fuel Process. Technol. 158 (2017) 130-140.

674 http://dx.doi.org/10.1016/j.fuproc.2016.12.015

675 [17] M.P. Kohn, M.J. Castaldi, R.J. Farrauto, Auto-thermal and dry reforming of landfill

676 gas over a Rh/γ-Al_2O_3 monolith catalyst, Appl. Catal. B 94 (2010) 125-133.

677 http://dx.doi.org/10.1016/j.apcatb.2009.10.029

678 [18] H. Kim, Y.-W. You, I. Heo, T.-S. Chang, J.S. Hong, K.B. Lee, J. K. Suh,

679 Development of monolithic catalyst system with Co-Ru-Zr for CO_2 (dry) reforming of

680 methane: Enhanced coke tolerance, Clean Technol. 23(3) (2017) 314-324.

681 http://dx.doi.org/10.7464/ksct.2017.23.3.314

682 [19] C. Fukuhara, R. Hyodo, K. Yamamoto, K. Masuda, R. Watanabe, A novel nickel-

683 based catalyst for methane dry reforming: a metal honeycomb-type catalyst prepared by

684 sol-gel method and electroless plating, Appl. Catal. A 468 (2013) 18-25.

685 http://dx.doi.org/10.1016/j.apcata.2013.08.024

686 [20] J.M. Leimert, J. Karl, M. Dillig, Dry reforming of methane using a nickel membrane

687 reactor, Processes 5(82) (2017) 1-13. http://dx.doi.org/10.3390/pr5040082

688 [21] A. Cybulski, J.A. Moulijn, Structured Catalysts and Reactors, Marcel Dekker, Inc.,

689 New York, 1998.

690 [22] T. Giroux, S. Hwang, Y. Liu, W. Ruettinger, L. Shore, Monolithic structures as

691 alternatives to particulate catalysts for the reforming of hydrocarbons for hydrogen

692   generation, Appl. Catal. B 56 (2005) 95-110.

693   http://dx.doi.org/10.1016/j.apcatb.2004.07.013

694   [23] C. Fukuhara, K. Hayakawa, Y. Suzuki, R. Watanabe, A novel nickel-based

695   structured catalyst for CO_2 methanation: a honeycomb-type Ni/CeO_2 catalyst to transform

696   greenhouse gas into useful resources. Appl. Catal. A 532 (2017) 12-18.

697   http://dx.doi.org/10.1016/j.apcata.2016.11.036

698   [24] S. Ratchahat, M. Sudoh, Y. Suzuki, W. Kawasaki, R. Watanabe, C. Fukuhara,

699   Development of a powerful CO_2 methanation process using a structured Ni/CeO_2 catalyst,

700   J. CO_2 Utilization 24 (2018) 210-219. https://doi.org/10.1016/j.jcou.2018.01.004

701   [25] J.M. Lavoie, Review on dry reforming of methane, a potentially more

702   environmentally-friendly approach to the increasing natural gas exploitation, Front.

703   Chem. 2(81) (2014) 1-17. http://dx.doi.org/10.3389/fchem.2014.00081

704   [26] J.C. Hernández-Garrido, D.M. Gómez, D. Gaona, H. Vidal, J.M. Gatica, O. Sanz,

705   J.M. Rebled, F. Peiró, J. J. Calvino, Combined (S)TEM-FIB insight into the influence of

706   the preparation method on the final surface structure of a Co_3O_4/La-modified-CeO_2

707   washcoated monolithic catalyst, J. Phys. Chem. C 117 (2013) 13028-13036.

708   http://dx.doi.org/10.1021/jp400151y

709   [27] J.C. Hernández-Garrido, D. Gaona, D.M. Gómez, J.M. Gatica, H. Vidal, O. Sanz,

710   J.M. Rebled, F. Peiró, J. J. Calvino, Comparative study of the catalytic performance and

711   final surface structure of Co_3O_4/La-CeO_2 washcoated ceramic and metallic honeycomb

712   monoliths, Catal. Today 253 (2015) 190-198.

713   http://dx.doi.org/10.1016/j.cattod.2015.01.035

714 [28] F. Agueniou, H. Vidal, M.P. Yeste, J.C. Hernández-Garrido, M.A. Cauqui, J.M.

715 Rodríguez-Izquierdo, J.J. Calvino, J.M. Gatica, Ultrathin washcoat and very low loading

716 monolithic catalyst with outstanding activity and stability in dry reforming of methane,

717 Nanomaterials 10(3) (2020) 445. http://dx.doi.org/10.3390/nano10030445

718 [29] M.P. Yeste, J.C. Hernandez-Garrido, D.C. Arias, G. Blanco, J.M. Rodríguez-

719 Izquierdo, J.M. Pintado, S. Bernal, J.A. Pérez-Omil, J.J. Calvino, Rational design of

720 nanostructured, noble metal free, ceria-zirconia catalysts with outstanding low

721 temperature oxygen storage capacity, J. Mater. Chem. A 1 (2013) 4836-4844.

722 http://dx.doi.org/10.1039/c3ta00016h

723 [30] D.M. Gómez, J.M. Gatica, J.C. Hernández-Garrido, G.A. Cifredo, M. Montes, O.

724 Sanz, J.M. Rebled, H. Vidal, A novel CoO_x/La-modified-CeO_2 formulation onto

725 cordierite honeycomb catalysts with application in VOCs oxidation, Appl. Catal. B 144

726 (2014) 425-434. http://dx.doi.org/10.1016/j.apcatb.2013.07.045

727 [31] O. Deutschmann, S. Tischer, S. Kleditzsch, V. Janardhanan, C. Correa, D.

728 Chatterjee, N. Mladenov, H. D. Minh, H. Karadeniz, M. Hettel, V. Menon

729 DETCHEM Software package, 2.7 ed., www.detchem.com, Karlsruhe 2018.

730 [32] K.S.W. Sing, D.H. Everett, R.A.W. Haul, L. Moscou, R.A. Pierotti, J. Rouquérol, T.

731 Siemieniewska, Reporting physisorption data for gas/solid systems with special reference

732 to the determination of surface area and porosity, Pure Appl. Chem. 57(4) (1985) 603-

733 619. https://doi.org/10.1515/iupac.57.0007

734 [33] J.M. Gatica, J. Castiglioni, C. de los Santos, M.P. Yeste, G. Cifredo, M. Torres, H.

735 Vidal, Use of pillared clays in the preparation of washcoated clay honeycomb monoliths

as support of manganese catalysts for the total oxidation of VOCs, Catal. Today 296 (2017) 86-94. http://dx.doi.org/10.1016/j.cattod.2017.04.025

[34] M. Yashima, T. Hirose, M. Kakihana, Y. Suzuki, M. Yoshimura, Size and charge effects of dopant M on the unit-cell parameters of monoclinic zirconia solid solutions $Zr_{0.98}M_{0.02}O_{2-\delta}$ (M = Ce, La, Nd, Sm, Y, Er, Yb, Sc, Mg, Ca), J. Am. Ceram. Soc. 80(1) (1997) 171-175. https://doi.org/10.1111/j.1151-2916.1997.tb02806.x

[35] J. Kaspar, P. Fornasiero, Structural properties and thermal stability of ceria-zirconia and related materials, in Catalytic Science Series: Vol. 2: Catalysis by ceria and related materials, A. Trovarelli (Ed.), Imperial College Press, London, 2002.

[36] A. Kambolis, H. Matralis, A. Trovarelli, Ch. Papadopoulou, Ni/CeO_2-ZrO_2 catalysts for the dry reforming of methane Appl. Catal. A 377 (2010) 16-26. https://doi.org/10.1016/j.apcata.2010.01.013

[37] H.-S. Roh, H.S. Potdar, K.-W. Jun, J.-W. Kim, Y.-S. Oh, Carbon dioxide reforming of methane over Ni incorporated into Ce–ZrO_2 catalysts, Appl. Catal. A 276 (2004) 231-239. https://doi.org/10.1016/j.apcata.2004.08.009

[38] J.A. Montoya, E. Romero-Pascual, C. Gimon, P. Del Angel, A. Monzon, Methane reforming with CO_2 over Ni/ZrO_2–CeO_2 catalysts prepared by sol–gel, Catal. Today 63 (2000) 71-85. https://doi.org/10.1016/S0920-5861(00)00447-8

[39] J. Chen, Q. Wu, J. Zhang, J. Zhang, Effect of preparation methods on structure and performance of $Ni/Ce_{0.75}Zr_{0.25}O_2$ catalysts for CH_4–CO_2 reforming, Fuel 87 (2008) 2901-2907. https://doi.org/10.1016/j.fuel.2008.04.015

757 [40] Z. Shang, S. Li, L. Li, G. Liu, X. Liang, Highly active and stable alumina supported

758 nickel nanoparticle catalysts for dry reforming of methane, Appl. Catal. B 201 (2017)

759 302-309. http://dx.doi.org/10.1016/j.apcatb.2016.08.019

760 [41] P. Kim, J.B. Joo, H. Kim, W. Kim, Y. Kim, I.K. Song, J. Yi, Preparation of

761 mesoporous Ni–alumina catalyst by one-step sol–gel method: control of textural

762 properties and catalytic application to the hydrodechlorination of o-dichlorobenzene,

763 Catal. Lett. 104(3–4) (2005) 181-189. http://dx.doi.org/10.1007/s10562-005-7949-5

764 [42] A. Iriondo, V.L. Barrio, J.F. Cambra, P.L. Arias, M.B. Guemez, M.C. Sanchez-

765 Sanchez, R.M. Navarro, J.L.G. Fierro, Glycerol steam reforming over Ni catalysts

766 supported on ceria and ceria-promoted alumina, Int. J. Hydrogen Energy 35 (2010)

767 11622-11633. http://dx.doi.org/10.1016/j.ijhydene.2010.05.105

768 [43] J.C. Escritori, S.C. Dantas, R.R. Soares, C.E. Hori, Methane autothermal reforming

769 on nickel–ceria–zirconia based catalysts, Catal. Commun. 10 (2009) 1090-1094. .

770 http://dx.doi.org/ 10.1016/j.catcom.2009.01.001

771 [44] S. Narayanan, K. Uma, Studies of the effect of calcination on the dispersion and

772 reduction of nickel supported on alumina by X-ray photoelectron spectroscopy, X-ray

773 diffraction, chemisorption and catalytic activity, J. Chem. Soc. Faraday Trans. 81 (1985)

774 2733-2736. https://doi.org/10.1039/F19858102733

775 [45] Y. Wang, L. Yao, S. Wang, D. Mao, C. Hu, Low-temperature catalytic CO_2 dry

776 reforming of methane on Ni-based catalysts: A review, Fuel Process. Technol. 169 (2018)

777 199-206. http://dx.doi.org/10.1016/j.fuproc.2017.10.007

778   [46] L. Smolakova, M. Kout, L.Capek, A. Rodriguez-Gomez, V.M. Gonzalez-Delacruz,

779   L. Hromadko, A. Caballero, Nickel catalyst with outstanding activity in the DRM reaction

780   prepared by high temperature calcination treatment, Int. J. Hydrogen Energy 41 (2016)

781   8459-8469. http://dx.doi.org/10.1016/j.ijhydene.2016.03.161

782   [47] C. Hoang-Van, Y. Kachaya, S.J. Teichner, Y. Amaud, J.A. Dalmon, Characterization

783   of nickel catalysts by chemisorption techniques, X-ray diffraction and magnetic

784   measurements: effects of support, precursor and hydrogen pretreatment, Appl. Catal. 46

785   (1989) 281-296. https://doi.org/10.1016/S0166-9834(00)81123-9

786   [48] J.S. Smith, P.A. Thrower, M.A. Vannice, Characterization of Ni/TiO_2, Catalysts by

787   TEM, X-Ray Diffraction, and Chemisorption Techniques, J. Catal. 68 (1981) 270-285.

788   https://doi.org/10.1016/0021-9517(81)90097-X

789   [49] T.A. Nijhuis, A.E.W. Beers, T. Vergunst, I. Hoek, F. Kapteijn, J.A. Moulijn,

790   Preparation of monolithic catalysts, Catal. Rev. –Sci. Eng. 43(4) (2001) 345-380.

791   https://doi.org/10.1081/CR-120001807

792   [50] D. Wu, S. Kong, Y. Li, H. Zhang, Mechanical stability of monolithic catalysts:

793   factors affecting washcoat adhesion and cohesion during preparation, AIChE J. 60(8)

794   (2014) 2765-2773. https://doi.org/10.1002/aic.14480

795   [51] L.A. Giannuzzi, F.A. Stevie, A review of focused ion beam milling techniques for

796   TEM   specimen   preparation,   Micron   30(3)   (1999)   197-204.

797   https://doi.org/10.1016/S0968-4328(99)00005-0

798   [52] W.-J. Jang, D.-W. Jeong, J.-O. Shim, H.-M. Kim, H.-S. Roh, I.H. Son, S.J. Lee,

799   Combined steam and carbon dioxide reforming of methane and side reactions:

800   Thermodynamic equilibrium analysis and experimental application, Appl. Energy 173

801   (2016) 80-91. http://dx.doi.org/10.1016/j.apenergy.2016.04.006

802   [53] S. Wang, G.Q. Lu, G.J. Millar, Carbon dioxide reforming of methane to produce

803   synthesis gas over metal-supported catalysts: State of the art, Energy & Fuels 10 (1996)

804   896-904. https://doi.org/10.1021/ef950227t

805   [54] M.K. Nikoo, N.A.S. Amin, Thermodynamic analysis of carbon dioxide reforming of

806   methane in view of solid carbon formation, Fuel Process. Technol. 92 (2011) 678-691.

807   https://doi.org/10.1016/j.fuproc.2010.11.027

808   [55] A. Serrano-Lotina, L. Daza, Influence of the operating parameters over dry

809   reforming of methane to syngas, Int. J. Hydrogen Energy 39 (2014) 4089-4094.

810   https://doi.org/10.1016/j.ijhydene.2013.05.135

811   [56] M.S. Fan, A.Z. Abdullah, S. Bhatia, Utilization of greenhouse gases through dry

812   reforming: screening of nickel-based bimetallic catalysts and kinetic studies, Chem. Sus.

813   Chem. 4 (2011) 1643-1653. https://doi.org/10.1002/cssc.201100113

814   [57] A.S.A. Al–Fatish, A.A. Ibrahim, A.H. Fakeeha, M.A. Soliman, M.R.H. Siddiqui,

815   A.E. Abasaeed, Coke formation during CO_2 reforming of CH_4 over alumina-supported

816   nickel   catalysts,   Appl.   Catal.   A   364   (2009)   150–155.

817   https://doi.org/10.1016/j.apcata.2009.05.043

818   [58] J. Newnham, K. Mantri, M.H. Amin, J. Tardio, S.K. Bhargava, Highly stable and

819   active Ni-mesoporous alumina catalysts for dry reforming of methane, Int. J. Hydrogen

820   Energy 37 (2012) 1454-1464. https://doi.org/10.1016/j.ijhydene.2011.10.036

821   [59] K. Tao, L. Shi, Q. Ma, D. Wang, C. Zeng, C. Kong, M. Wu, L. Chen, S. Zhou, Y.

822   Hu, N. Tsubaki, Methane reforming with carbon dioxide over mesoporous nickel–

823   alumina composite catalyst, Chem. Eng. J. 221 (2013) 25–31.

824   https://doi.org/10.1016/j.cej.2013.01.073

825   [60] G. Zhang, J. Liu, Y. Xu, Y. Sun, A review of CH_4-CO_2 reforming to synthesis gas

826   over Ni-based catalysts in recent years (2010-2017), Int. J. Hydrogen Energy 43 (2018)

827   15030-15054. https://doi.org/10.1016/j.ijhydene.2018.06.091

828   [61] T. Yabe, Y. Sekine, Methane conversion using carbon dioxide as an oxidizing agent:

829   A review, Fuel Process. Technol. 181 (2018) 187-198.

830   https://doi.org/10.1016/j.fuproc.2018.09.014